photonics

MDPI

Article

Single Scattering Dynamics of Vector Bessel–Gaussian Beams in Winter Haze Conditions

Yixiang Yang [1], Yuancong Cao [2], Wenjie Jiang [2], Lixin Guo [2] and Mingjian Cheng [2,*]

[1] School of Physics and Mechanics, Wuhan University of Technology, Wuhan 430070, China; yxyang_optic@163.com
[2] School of Physics, Xidian University, Xi'an 710071, China; 24201111388@stu.xidian.edu.cn (Y.C.); 23201214857@stu.xidian.edu.cn (W.J.); lxguo@xidian.edu.cn (L.G.)
* Correspondence: mjcheng@xidian.edu.cn

Abstract: This study investigates the scattering dynamics of vector Bessel–Gaussian (BG) beams in winter haze environments, with a particular emphasis on the influence of ice-coated haze particles on light propagation. Employing the Generalized Lorenz–Mie Theory (GLMT), we analyze the scattering coefficients of particles transitioning from water to ice coatings under varying atmospheric conditions. Our results demonstrate that the presence of ice coatings significantly alters the scattering and extinction efficiencies of BG beams, revealing distinct differences compared to particles coated with water. Furthermore, the study examines the role of Orbital Angular Momentum (OAM) modes in shaping scattering behavior. We show that higher OAM modes, characterized by broader energy distributions and larger beam spot sizes, induce weaker localized interactions with individual particles, leading to diminished scattering and attenuation. In contrast, lower OAM modes, with energy concentrated in smaller regions, exhibit stronger interactions with particles, thereby enhancing scattering and attenuation. These findings align with the Beer–Lambert law in the single scattering regime, where beam intensity attenuation is influenced by the spatial distribution of radiation, while overall power attenuation follows the standard exponential decay with respect to propagation distance. The transmission attenuation of BG beams through haze-laden atmospheres is further explored, emphasizing the critical roles of particle concentration and humidity. This study provides valuable insights into the interactions between vector BG beams and atmospheric haze, advancing the understanding of optical communication and environmental monitoring in hazy conditions.

Keywords: structured light; scattering and transmission; hazy atmospheres

check for updates

Received: 2 January 2025
Revised: 10 February 2025
Accepted: 20 February 2025
Published: 22 February 2025

Citation: Yang, Y.; Cao, Y.; Jiang, W.; Guo, L.; Cheng, M. Single Scattering Dynamics of Vector Bessel–Gaussian Beams in Winter Haze Conditions. *Photonics* **2025**, *12*, 182. https://doi.org/10.3390/photonics12030182

Copyright: © 2025 by the authors. Licensee MDPI, Basel, Switzerland. This article is an open access article distributed under the terms and conditions of the Creative Commons Attribution (CC BY) license (https://creativecommons.org/licenses/by/4.0/).

1. Introduction

The interaction between light and the atmosphere is fundamental to physical optics and has significant implications for fields such as optical communication, environmental monitoring, and remote sensing [1]. This interaction is influenced by the atmosphere's complex composition, which includes various gases, water vapor, and aerosols, resulting in scattering, absorption, and refraction phenomena [2]. In particular, haze conditions, characterized by an increase in particulate matter, complicate atmospheric optics, creating substantial challenges for beam stability and signal fidelity. A deeper understanding of these interactions is crucial not only for advancing the design of optical systems but also for improving applications in weather forecasting and climate research [3,4].

The Mie theory, which models light scattering by spherical particles, provides a fundamental framework for understanding light-particle interactions [5]. Originally developed

by Lorenz [6] and Mie [7], this theory offers analytical solutions for scattering based on the particle's diameter and composition. It has become the theoretical basis for investigating atmospheric scattering phenomena [8]. However, the inherent variability in the size, refractive index, and composition of atmospheric haze particles, ranging from hygroscopic tropospheric particles to stratospheric dust, smoke, sulfate particles, and volcanic ash, presents a significant challenge [9,10], as depicted in Figure 1a. Additionally, atmospheric water vapor plays a pivotal role in modulating particle size, particularly under varying humidity conditions [11]. At high humidity levels, haze particles absorb water [12], forming complex multilayered structures that require extensions to the classic Mie theory, such as models incorporating concentric spherical layers [13]. This issue is especially relevant in seasonal haze regions, where particles may develop ice coatings under colder conditions, further complicating the scattering dynamics [14].

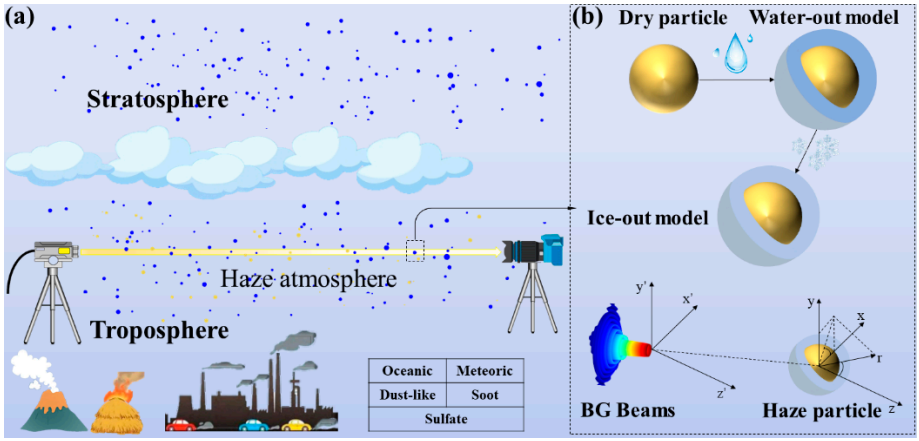

Figure 1. (**a**) Transmission schematic of BG beams in haze environment. (**b**) Ice-coated haze particles corrected model and schematic of BG beam particle scattering.

In the design of optical systems intended for deployment in challenging atmospheric conditions, it is essential to investigate the behavior of structured light beams [15], including Airy beams and Bessel–Gaussian (BG) beams. Airy beams are particularly noteworthy for their self-accelerating and refocusing properties, which have shown potential in mitigating scattering effects and preserving beam integrity in nonlinear media [16]. Vortex beams, which manipulate the wavefront through orbital angular momentum (OAM), have demonstrated their utility in various atmospheric applications [17]. Recent studies have advanced our understanding of vortex beam dynamics, encompassing the spatiotemporal control of plasmonic vortices [18], robust OAM measurements in partially coherent vortex beams under perturbations [19], and the functional multiplexing in high-efficiency metasurfaces based on coherent wave interference [20]. Among these, BG beams stand out for their unique characteristics, including non-diffraction, self-reconstruction, and inherent resilience to scattering. These attributes make them particularly well-suited for a wide range of applications, such as optical communication [21,22], OAM holography [23], rotating object detection [24], particle trapping [25], and beyond [26]. However, while BG beams are capable of self-healing when obstructed by isolated obstacles, atmospheric turbulence and scattering affect all incident conical waves, severely undermining their self-reconstruction capability [27].

The robustness of BG beams has been widely studied in the context of various environmental disturbances, including turbulence [28], marine aerosols [29], dust [30], and rainfall [31]. Their ability to maintain beam integrity under these challenging conditions highlights their potential for use in atmospheric communication systems. However, despite these advantages, the scattering behavior of BG beams in hazy atmospheres, characterized

by a complex interplay of particle sizes, refractive indices, and environmental factors, remains insufficiently explored. This study aims to address this gap by investigating the single scattering dynamics of vector BG beams under typical winter haze conditions. Specifically, it examines how haze particles influence light propagation and assesses the effects of particle size and concentration on the scattering and transmission properties of BG beams. While real-world atmospheric conditions involve intricate interactions between scattering, turbulence, and other phenomena, this study employs a simplified numerical model to establish a foundation for future experimental research. By simulating the scattering of a single BG beam in the presence of haze particles, we seek to provide valuable insights into the impact of atmospheric scattering on optical communication systems, paving the way for subsequent investigations in more complex atmospheric environments.

2. Theoretical Model

The GLMT offers a framework for characterizing the scattering behavior of structured light beams interacting with spherical particles [32]. In this framework, the resulting scattered field is expressed in terms of spherical vector wave functions (SVWFs), which are modulated by the beam shape coefficients (BSCs) [33]:

$$\begin{cases} \mathbf{E}_s = \sum\limits_{n=1}^{\infty} \sum\limits_{m=-n}^{n} c_n^m \left[A_n^m \mathbf{N}_{mn}^{(3)}(k\mathbf{r}) + \mathrm{i} B_n^m \mathbf{M}_{mn}^{(3)}(k\mathbf{r}) \right] \\ \mathbf{H}_s = -\dfrac{\mathrm{i}k}{\omega\mu_0} \sum\limits_{n=1}^{\infty} \sum\limits_{m=-n}^{n} c_n^m \left[A_n^m \mathbf{M}_{mn}^{(3)}(k\mathbf{r}) + \mathrm{i} B_n^m \mathbf{N}_{mn}^{(3)}(k\mathbf{r}) \right] \end{cases} \tag{1}$$

where $\mathbf{M}_{mn}^{(3)}(k\mathbf{r})$ and $\mathbf{N}_{mn}^{(3)}(k\mathbf{r})$ denote SVWFs, $\mathbf{r}$ represents the position vector, and k is the wavenumber, related to wavelength λ by $k = 2\pi/\lambda$, ω is the angular frequency, μ_0 denotes the magnetic permeability of free space, and the term c_n^m is expressed as [29]:

$$c_n^m = \begin{cases} \mathrm{i}^{n-1} \frac{2n+1}{n(n+1)} & m \geq 0 \\ (-1)^{|m|} \frac{(n+|m|)!}{(n-|m|)!} \mathrm{i}^{n-1} \frac{2n+1}{n(n+1)} & m < 0 \end{cases} \tag{2}$$

The terms A_n^m and B_n^m represent the expansion coefficients of the scattered field for the interaction between the BG beam and a single spherical particle, which are derived from the boundary conditions [33]:

$$\begin{cases} A_n^m = a_n g_{n,TM}^m \\ B_n^m = b_n g_{n,TE}^m \end{cases} \tag{3}$$

where the classical Mie scattering coefficients a_n and b_n describe the scattering behavior of a spherical particle in terms of its response to a plane wave incident from a specified direction. These coefficients depend on the wavelength of the light, the size of the particle, and the optical properties of the particle (e.g., refractive index).

2.1. The BSCs of BG Beams

Consider a vector BG beam propagating along the z-axis, illuminating a concentric spherical particle with an inner radius a, outer radius b, and refractive indices m_1 and m_2. The surrounding medium is assumed to be vacuum. The incident beam is positioned in the coordinate system o′x′y′z′, with its center at o′. For the particle, the corresponding coordinate system is oxyz, with its center at o. The coordinates of o′ in the oxyz system are (x_0, y_0, z_0). The electric field of the vector BG beam is expressed through the angular spectrum expansion method as follows [29]:

$$\mathbf{E}(\mathbf{r}) = \frac{k^2}{4\pi^2} \int_0^{2\pi} \int_0^{\frac{\pi}{2}} \mathbf{e}_u E_k(\alpha, \beta) \exp(\mathrm{i}\mathbf{k}\cdot\mathbf{r} + \mathrm{i}\mathbf{k}\cdot\mathbf{r}_0) \sin\alpha \cos\alpha \mathrm{d}\alpha \mathrm{d}\beta \tag{4}$$

where $\mathbf{r}_0 = (x_0, y_0, z_0)$ is the center of incident beam, $E_k(\alpha, \beta)$ is the angular spectrum of the BG beam, and the wavevector is given by $\mathbf{k} = (k_x, k_y, k_z)$, with components $k_x = k_\rho \cos\beta$, $k_y = k_\rho \sin\beta$, $k_z = k\cos\alpha$, and $k_\rho = k\sin\alpha$. Here, α and β denote the angles between the wavevector of the plane wave components and the coordinate axes of the particle in the particle's coordinate system.

$$\mathbf{e}_u = \rho_x \mathbf{e}_\mathbf{x} + \rho_y \mathbf{e}_\mathbf{y} \tag{5}$$

The polarization state of a vector beam is represented by the unit vector $\mathbf{e}_u = (\rho_x, \rho_y)$, where ρ_x and ρ_y correspond to the polarization components along the x- and y-axes, respectively. For vector BG beams with different polarization states, the values of $\mathbf{e}_u$ vary. Some typical polarization states are as follows: (1, 0) for linear x-polarization; (0, 1) for linear y-polarization; (1, i) for left circular polarization; (1, −i) for right circular polarization; (cosβ, sinβ) for radial polarization; and (−sinβ, cosβ) for azimuthal polarization.

The BSCs $\left(g_{n,TM}^{m,u}, g_{n,TE}^{m,u}\right)$ of the higher-order BG beam are given by [29]:

$$g_{n,TM}^{m,u} = \begin{cases} \frac{n(n+1)}{\mathrm{i}^{n+1}(2n+1)} q_{mn}^u & m \geq 0 \\ \frac{1}{(-1)^{|m|}\mathrm{i}^{n+1}} \frac{(n+m)!}{(n-m)!} \frac{n(n+1)}{(2n+1)} q_{mn}^u & m < 0 \end{cases} \tag{6}$$

$$g_{n,TE}^{m,u} = \begin{cases} \frac{n(n+1)}{-\mathrm{i}^{n}(2n+1)} p_{mn}^u & m \geq 0 \\ \frac{1}{(-1)^{|m|}\mathrm{i}^{n}} \frac{(n+m)!}{(n-m)!} \frac{n(n+1)}{(2n+1)} p_{mn}^u & m < 0 \end{cases} \tag{7}$$

To determine the waveform factors of vector higher-order BG beams under different polarization states, it suffices to derive the coefficients p_{mn}^u and q_{mn}^u for each polarization state. For instance, in the case of a linearly x-polarized vector BG beam, the coefficients p_{mn}^x and q_{mn}^x are expressed as [29]:

$$\begin{aligned} \begin{Bmatrix} p_{mn}^x \\ q_{mn}^x \end{Bmatrix} &= A \int_0^{\frac{\pi}{2}} \exp\left[-\frac{{w_0}^2}{4}\left(k_\rho^2 + \gamma^2\right)\right] I_s\left(\frac{k_\rho \gamma {w_0}^2}{2}\right) \\ &\times \begin{Bmatrix} \cos\alpha I_+ \pi_{mn}(\cos\alpha) + \mathrm{i} I_- \tau_{mn}(\cos\alpha) \\ \cos\alpha I_+ \tau_{mn}(\cos\alpha) + \mathrm{i} I_- \pi_{mn}(\cos\alpha) \end{Bmatrix} \sin\alpha \cos\alpha \mathrm{d}\alpha \end{aligned} \tag{8}$$

Here, w_0 is the beam width, $\gamma = k\sin\theta_b$ represents the wave parameter, θ_b is the cone angle of the beam, s denotes the OAM mode number, and $I_j(x)$ represents the modified Bessel function of the first kind of order j.

$$A = (-1)^{l+1}\mathrm{i}^{n+1}{w_0}^2 \frac{k^2}{\pi} \frac{(2n+1)(n-m)!}{4n(n+1)(n+m)!} \exp\left(\frac{\mathrm{i}s\pi}{2}\right) \tag{9}$$

$$\pi_n^m(\cos\theta) = mP_n^m(\cos\theta)/\sin\theta \tag{10}$$

$$\tau_n^m(\cos\theta) = \mathrm{d}P_n^m(\cos\theta)/\mathrm{d}\theta \tag{11}$$

$$I_+ = \pi \exp(\mathrm{i}k\cos\alpha z_0) \begin{Bmatrix} J_{m-s-1}(k_\rho\rho_0) \exp\left[\mathrm{i}(s-m+1)\varphi_0 + \mathrm{i}(m-s-1)\frac{\pi}{2}\right] \\ +J_{m-s+1}(k_\rho\rho_0) \exp\left[\mathrm{i}(s-m-1)\varphi_0 + \mathrm{i}(m-s+1)\frac{\pi}{2}\right] \end{Bmatrix} \tag{12}$$

$$I_- = \mathrm{i}\pi \exp(\mathrm{i}k\cos\alpha z_0) \begin{Bmatrix} J_{m-s+1}(k_\rho\rho_0) \exp\left[\mathrm{i}(s-m-1)\varphi_0 + \mathrm{i}(m-s+1)\frac{\pi}{2}\right] \\ -J_{m-s-1}(k_\rho\rho_0) \exp\left[\mathrm{i}(s-m+1)\varphi_0 + \mathrm{i}(m-s-1)\frac{\pi}{2}\right] \end{Bmatrix} \tag{13}$$

with $\rho_0 = \sqrt{x_0^2 + y_0^2}$, $\varphi_0 = \arctan(y_0/x_0)$. Additionally, $P_n^m(\cos\theta)$ is the associated Legendre polynomial of order n and degree m, given by:

$$P_n^m(\cos\theta) = (-1)^m \left(1 - x^2\right)^{m/2} \frac{\mathrm{d}^m}{\mathrm{d}x^m} \left(x^2 - 1\right)^n \tag{14}$$

For other polarization states, the coefficients p_{mn}^u and q_{mn}^u can be found in Ref. [29].

2.2. The Single Scattering Model of BG Beams with Ice-Coating Haze Particles

For a concentric spherical particle, the Mie coefficients a_n and b_n can be expressed in terms of the Riccati–Bessel functions as follows [11]:

$$a_n = \frac{H_n^{(a)} \psi_n(ka) - m_r \psi'_n(ka)}{H_n^{(a)} \xi_n^{(1)}(ka) - m_r \xi'^{(1)}_n(ka)} \tag{15}$$

$$b_n = \frac{m_r H_n^{(b)} \psi_n(ka) - \psi'_n(ka)}{m_r H_n^{(b)} \xi_n^{(1)}(ka) - \xi'^{(1)}_n(ka)} \tag{16}$$

$$H_n^{(a)} = \frac{Q_n^d \xi'^{(1)}_n(k_1 a) + \xi'^{(2)}_n(k_1 a)}{Q_n^d \xi_n^{(1)}(k_1 a) + \xi_n^{(2)}(k_1 a)} \tag{17}$$

$$H_n^{(b)} = \frac{Q_n^c \xi'^{(1)}_n(k_1 a) + \xi'^{(2)}_n(k_1 a)}{Q_n^c \xi_n^{(1)}(k_1 a) + \xi_n^{(2)}(k_1 a)} \tag{18}$$

$$Q_n^d = \frac{k_1 \xi_n^{(2)}(k_1 b) \psi'_n(k_2 b) - k_2 \xi'^{(2)}_n(k_1 b) \psi_n(k_2 b)}{k_2 \xi'^{(1)}_n(k_1 b) \psi_n(k_2 b) - k_1 \xi_n^{(1)}(k_1 b) \psi'_n(k_2 b)} \tag{19}$$

$$Q_n^c = \frac{k_1 \xi'^{(2)}_n(k_1 b) \psi_n(k_2 b) - k_2 \xi_n^{(2)}(k_1 b) \psi'_n(k_2 b)}{k_2 \xi_n^{(1)}(k_1 b) \psi'_n(k_2 b) - k_1 \xi'^{(1)}_n(k_1 b) \psi_n(k_2 b)} \tag{20}$$

where $m_r = m_2/m_1$ is the relative refractive index of the outer layer of the spherical shell, k_1 and k_2 represent the wavenumbers corresponding to outer layer and shell. The functions $\psi_n(x)$, $\xi_n^{(1)}(x)$, and $\xi_n^{(2)}(x)$, and their derivatives $\psi'_n(x)$, $\xi'^{(1)}_n(x)$, and $\xi'^{(2)}_n(x)$ are the Riccati–Bessel functions of the first kind and their derivatives.

The origins of haze phenomena exhibit substantial regional and temporal variability, influenced by a range of factors. Among these, the variation in the complex refractive index of haze particles plays a crucial role in governing the differences in laser transmission across different haze conditions. Haze particles are typically categorized based on their core compositions, such as meteoric, dust, soot, and sulfate particles. The complex refractive index and density of these particles have a significant impact on their scattering behavior. Notably, the complex refractive index of haze particles is wavelength-dependent, as summarized in Table 1 [10].

Table 1. The complex refractive index of different haze particles' nucleus, as well as ice and water, and the i is the imaginary unit.

	Wavelength	**0.86 μm**	**1.06 μm**	**2 μm**	**5 μm**
Outer layer	Water	$1.329 + 3.29 \times 10^{-7}$i	$1.326 + 4.18 \times 10^{-6}$i	$1.306 + 1.10 \times 10^{-3}$i	$1.325 + 1.24 \times 10^{-2}$i
	Ice	$1.303 + 2.15 \times 10^{-7}$i	$1.300 + 1.96 \times 10^{-6}$i	$1.273 + 1.61 \times 10^{-3}$i	$1.327 + 1.20 \times 10^{-2}$i
Core	Meteoric	$1.509 + 1.02 \times 10^{-3}$i	$1.506 + 1.95 \times 10^{-3}$i	$1.482 + 1.51 \times 10^{-2}$i	1.5 + 0.135i
	Dust-type	$1.520 + 8 \times 10^{-3}$i	$1.520 + 8 \times 10^{-3}$i	$1.260 + 8 \times 10^{-3}$i	$1.25 + 1.26 \times 10^{-2}$i
	Soot	1.75 + 0.43i	1.75 + 0.44i	1.80 + 0.49i	1.97 + 0.60i
	Sulfate	$1.425 + 1.79 \times 10^{-7}$i	$1.420 + 1.5 \times 10^{-6}$i	$1.384 + 1.26 \times 10^{-3}$i	1.360 + 0.121i

For a concentric spherical particle illuminated by a vector BG beam, the differential scattering cross-section then can be computed, accounting for both the electric and magnetic field contributions to the scattering process. The radar cross-section (RCS), which describes the scattering of light in a specific direction, is defined as:

$$\sigma = \frac{\lambda^2}{\pi}\left(|S_1|^2 + |S_2|^2\right) \tag{21}$$

$$S_1 = \sum_{n=1}^{\infty}\sum_{m=-n}^{n} c_n^m [A_n^m \pi_{mn}(\cos\theta) + \mathrm{i}B_n^m \tau_{mn}(\cos\theta)] e^{\mathrm{i}m\varphi} \tag{22}$$

$$S_2 = \sum_{n=1}^{\infty}\sum_{m=-n}^{n} c_n^m [A_n^m \tau_{mn}(\cos\theta) + \mathrm{i}B_n^m \pi_{mn}(\cos\theta)] e^{\mathrm{i}m\varphi} \tag{23}$$

with

$$\begin{cases} \pi_{mn}(\cos\theta) = \frac{P_n^m(\cos\theta)}{\sin\theta} \\ \tau_{mn}(\cos\theta) = \frac{\mathrm{d}}{\mathrm{d}\theta} P_n^m(\cos\theta) \end{cases} \tag{24}$$

The extinction efficiency factor Q_{ext}, which characterizes the total extinction (scattering and absorption) per unit cross-sectional area, is given by:

$$Q_{sca} = \frac{4}{k^2 b^2}\sum_{n=1}^{\infty}\sum_{m=-n}^{n} \frac{2n+1}{n(n+1)}\frac{(n+|m|)!}{(n-|m|)!}\left(a_n \left|g_{n,TM}^m\right|^2 + b_n \left|g_{n,TE}^m\right|^2\right) \tag{25}$$

$$Q_{ext} = \frac{4}{k^2 b^2}\mathrm{Re}\left[\sum_{n=1}^{\infty}\sum_{m=-n}^{n} \frac{2n+1}{n(n+1)}\frac{(n+|m|)!}{(n-|m|)!}\left(a_n \left|g_{n,TM}^m\right|^2 + b_n \left|g_{n,TE}^m\right|^2\right)\right] \tag{26}$$

$$Q_{abs} = Q_{ext} - Q_{sca} \tag{27}$$

where b is the outer radius of the spherical particle.

2.3. Transmission Attenuation Model of BG Beam in Haze Environment

When the distribution of haze particles in the atmosphere is relatively sparse, with a significant distance between particles, two specific conditions can be used to approximate the scattering effects as independent. The first condition assumes that the separation between particles exceeds three times their diameter [34]. Alternatively, independence can be assumed if the distance between the edges of haze particles relative to the wavelength of the light beam is greater than 0.5 [35]. Under these conditions, the interaction between scattered particles is minimal, and only the single scattering effect is typically considered in the propagation of the BG beam between the transmitting and receiving devices, with multiple scattering effects being negligible.

The particle size distribution of haze significantly influences its attenuation characteristics for lasers. Currently, the most commonly used haze particle size distribution function is the modified gamma distribution proposed by Deirmendjian [36]:

$$f(r) = Cr^{\xi}\exp(-Dr^{\eta}) \tag{28}$$

where C, D, ξ, and η are constants, and r represents the radius of haze particles. In continental haze particles, when $N = 100/\mathrm{cm}^3$, $C = 4.98 \times 10^6$, $D = 15.1186$, $\xi = 2$, $\eta = 0.5$.

According to wave propagation and scattering theory in random media, for agglomerated particles following a size distribution, the attenuation rate due to a light beam traveling through the medium over a unit distance can be expressed as:

$$A(\lambda) = 0.008686\int_0^{r_{\max}} \pi r^2 Q_{ext}(r) f(r)\mathrm{d}r \ (dB/km) \tag{29}$$

By substituting Equation (25) into Equation (28), the signal attenuation rate of an incident vector BG beam can be derived as:

$$A(\lambda) = \frac{15\int_0^{r_{\max}} r^2 Q_{ext}(r) f(r) \mathrm{d}r}{V_b \int_0^{r_{\max}} r^2 f(r) \mathrm{d}r} \ (dB/km) \tag{30}$$

Further, based on the Beer–Lambert law, the atmospheric transmittance of the light beam over a horizontal transmission distance L (in kilometers) is given by:

$$\tau(\lambda, L) = \exp(-A(\lambda)L) \tag{31}$$

where L is the horizontal transmission distance in kilometers.

3. Numerical Calculations and Discussions

We investigated the scattering characteristics of vector BG beams interacting with various types of haze particles, including meteoric, dust-like, soot, and sulfate particles, each coated with either ice or water, based on their respective complex refractive index parameters. Figure 2 displays the RCS for these four haze particle types under X-polarized BG beam irradiation, highlighting two distinct coating conditions: ice (black line) and water (red line). The simulations were conducted with the following parameters: beam width w_0 = 5.18 μm, topological charge s = 2, cone angle θ_b = 25°, and wavelength λ = 1.06 μm. For water-coated particles, the inner-to-outer diameter ratio was a/b = 0.7, while for ice-coated particles, this ratio was derived based on the density of ice.

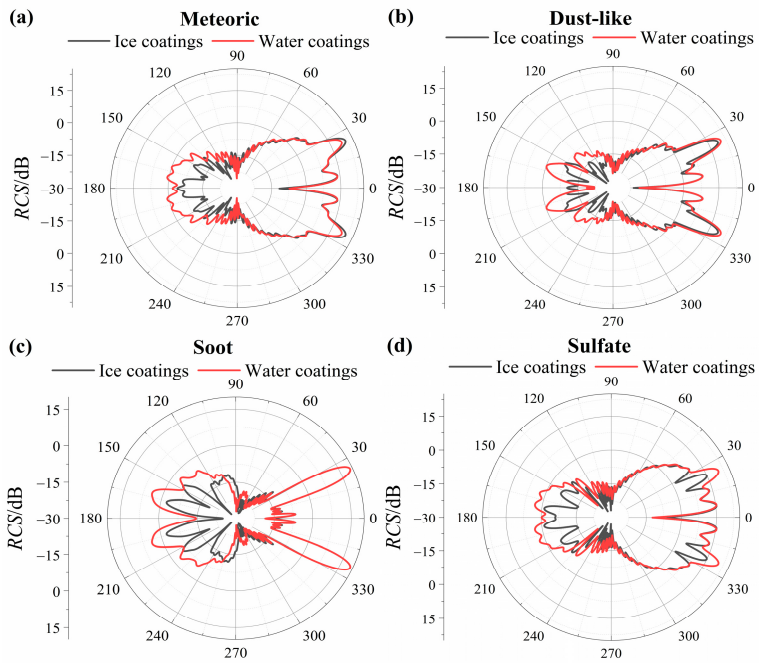

Figure 2. RCS of various haze particles with ice and water coatings under X-polarized BG beam irradiation: (**a**) meteoric-type particles, (**b**) dust-like particles, (**c**) soot particles, and (**d**) sulfate particles.

The results demonstrate the dependence of RCS on the surface refractive index, modulated by the coating material. A significant difference in scattering intensities is observed between ice- and water-coated particles, particularly in the angular range from 90° to 270°, where water-coated particles consistently exhibit higher RCS values. This disparity underscores the pivotal role of surface refractive properties and particle morphology in determining scattering behavior.

The transformation in surface refractive index and morphology due to ice coatings significantly affects scattering intensities, emphasizing the importance of incorporating ice-coated particles in models for accurate laser transmission predictions through haze. This is especially pertinent in colder winter conditions, where the transition of water to ice on haze particles becomes pronounced. Such transformations must be systematically integrated into haze scattering models, particularly in scenarios involving multiple scattering events, where a comprehensive angular distribution of scattered intensity is critical.

Figure 3 presents the RCS of soot-like haze particles coated with either ice or water when exposed to X-polarized BG beams carrying OAM modes s = 1 and s = 3. The RCS values, expressed in decibels (dB), are evaluated at four distinct wavelengths: 0.86 μm, 1.06 μm, 2.0 μm, and 5.0 μm. Despite having the same initial power for each OAM mode, the scattering indicatrices differ due to the varying intensity distributions of the BG beams. These beams generate interference patterns within the scattering volume that vary with the OAM mode, resulting in distinct angular scattering distributions for each case.

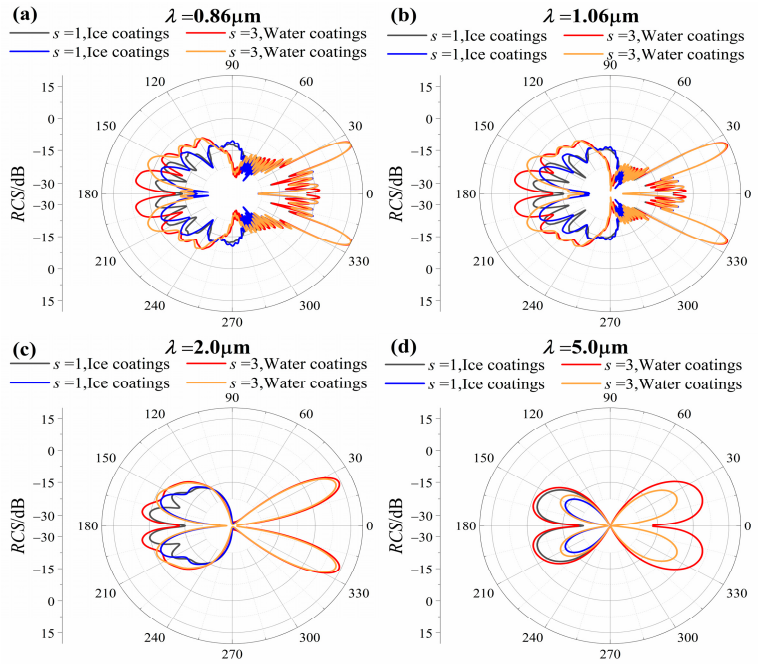

Figure 3. RCS of soot-type haze particles with ice and water coatings under linearly polarized BG beam irradiation featuring OAM modes s = 1 and s = 3: (**a**) λ = 0.86 μm, (**b**) λ = 1.06 μm, (**c**) λ = 2.0 μm, (**d**) λ = 5 μm.

For the s = 1 mode, the RCS remains consistently higher across all wavelengths, indicating a stronger interaction between the incident vortex beam and the particles. It is important to highlight that, while the shape and distribution of the RCS vary, the total integrated scattered power remains constant across different OAM modes, in accordance with the principle of energy conservation. The total scattered power corresponds to the integral of the RCS over the entire scattering volume. Consequently, variations in RCS do not signify a change in total scattered energy but rather a redistribution of this energy across different scattering angles. This redistribution arises from the unique intensity profiles and phase-front characteristics of each OAM mode, which govern the angular dependence of the scattering pattern while preserving the overall power.

As the wavelength increases, the RCS patterns transition from broader distributions to more localized structures, particularly for ice-coated particles. This evolution underscores the wavelength's influence on scattering dynamics, which is dictated by the interplay between particle size, refractive index contrast, and the incident wavelength. These factors

collectively shape the dominant scattering mechanisms, with shorter wavelengths exhibiting greater sensitivity to the particle coatings, while longer wavelengths demonstrate a more pronounced dependence on the OAM mode. Understanding these distinctions is essential for characterizing how scattering behaviors vary as a function of both the scatterers' physical properties (e.g., coating composition) and the characteristics of the incident light (e.g., wavelength and OAM mode).

For haze particles with a core-shell structure, the inner-to-outer sphere radius ratio is often considered a key factor influencing particle scattering. Figure 4 shows the RCS of soot-type haze particles with ice and water coatings for inner-to-outer diameter ratios a/b = 0.7 and a/b = 0.9 across various polarization states. The results indicate that the RCS values for water-coated particles (red and orange lines) are consistently higher than those for ice-coated particles (black and blue lines), suggesting a stronger scattering effect associated with the water coatings. However, the influence of the inner-to-outer diameter ratio on the RCS is minimal, with no significant change observed across the different ratios.

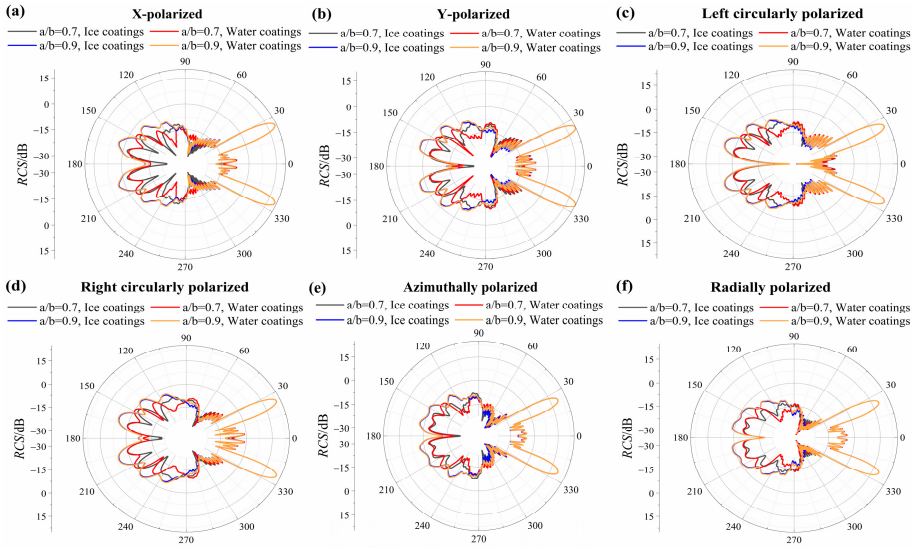

Figure 4. RCS of soot-type haze particles with ice and water coatings for various inner-to-outer diameter ratios (a/b = 0.7 and a/b = 0.9) under vector BG beam irradiation with different polarization states: (**a**) X-polarized, (**b**) Y-polarized, (**c**) left circularly polarized, (**d**) right circularly polarized, (**e**) azimuthally polarized, and (**f**) radially polarized.

All RCS distributions exhibit symmetry, with scattering intensity varying according to the orientation of the particle. The peak RCS values remain relatively consistent, with forward scattering predominantly concentrated in the 30° and 330° directions, aligning with the electric field orientation of the BG beam. In contrast, the backward scattering intensity distribution is more intricate, showing significant variations across different polarization states. These variations are indicative of the polarization characteristics of the electric field. Despite these differences, the overall symmetry of the RCS is maintained, and its magnitude remains largely unchanged. Radial and azimuthal polarization states exhibit a larger overall amplitude. Although the polarization state affects the angular scattering distribution, it does not notably alter the RCS magnitude, which is primarily determined by factors such as the coating material and its thickness.

Figure 5 presents the efficiency factors for soot-type haze particles coated with ice and water under X-polarized BG beam irradiation at wavelengths λ =0.86 μm and λ = 5.0 μm, offering valuable insights into their optical properties. The results reveal a strong wavelength dependence in the efficiency factors. At the longer wavelength of λ = 5.0 μm, all three efficiency factors are markedly lower than at λ = 0.86 μm, indicating a significant

reduction in radiative interactions at extended wavelengths. A distinct resonance peak near $x \approx 10$ highlights size-dependent absorption and scattering phenomena, modulated by both coating type and wavelength. While the RCS distributions differ between ice- and water-coated haze particles, the efficiency factors show only minor deviations, suggesting that the coating composition induces only subtle changes in the particles' optical properties. However, the overall consistency in efficiency factor trends emphasizes the stable optical response of these haze particles to variations in coating composition under the examined conditions.

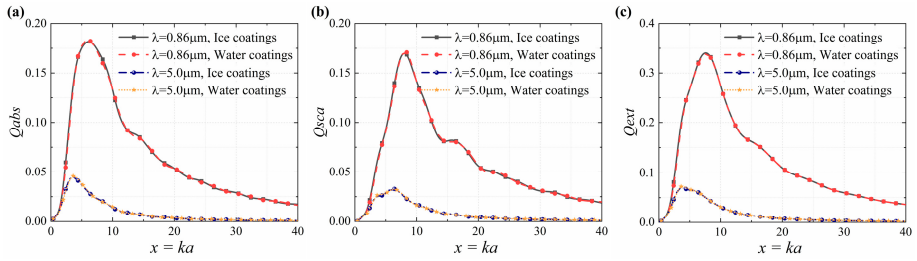

Figure 5. Efficiency factors of soot-type haze particles with ice and water coatings under X-polarized BG beam irradiation at wavelengths λ = 0.86 μm and λ = 5.0 μm: (**a**) absorption efficiency factor, (**b**) scattering efficiency factor, and (**c**) extinction efficiency factor.

Figure 6 illustrates the energy transmittance of X-polarized BG beams propagating through soot-type haze environments with varying particle concentrations (N = 5000, 10,000, 15,000, 20,000 cm^{-3}). As particle concentration increases, the frequency of scattering events rises sharply, leading to a pronounced reduction in transmittance. This decline is evident across both short and long wavelengths, with the effect becoming more pronounced at higher concentrations, where the increased particle density enhances both scattering and attenuation. Notably, longer wavelengths exhibit higher transmittance, in agreement with the Mie scattering theory, as they experience relatively less scattering due to their larger wavelength compared to the particle size. At the highest particle concentration (N = 20,000 cm^{-3}), transmittance diminishes significantly across all wavelengths, with shorter wavelengths (e.g., λ = 0.86 μm) exhibiting the most substantial reduction.

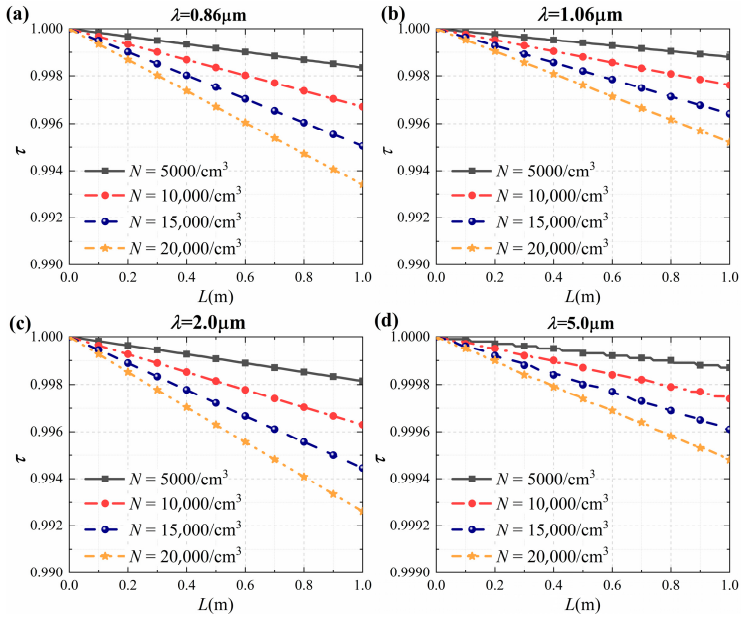

Figure 6. Transmittance of X-polarized BG beam at wavelengths λ = 0.86 μm (**a**), λ = 1.06 μm (**b**), λ = 2.0 μm (**c**), and λ = 5.0 μm (**d**) in soot-type haze environments with varying concentrations N = 5000, 10,000, 15,000, 20,000 cm^{-3}.

The transmission characteristics of X-polarized BG beams with various OAM modes (s = 0, 1, 2, and 3) propagating through haze environments composed of different particle types, including meteoric, dust-like, soot, and sulfate particles, are illustrated in Figure 7. Attenuation and scattering behaviors are influenced not only by the intrinsic properties of the particles (such as size, composition, and concentration) but also by the spatial energy distribution of the BG beam associated with each OAM mode.

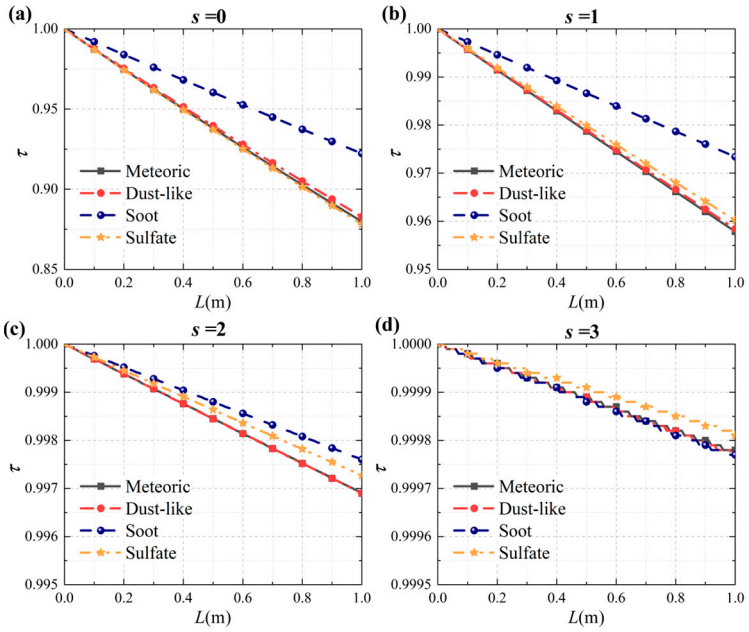

Figure 7. Transmittance of X-polarized BG beam with OAM modes m = 0 (**a**), m = 1 (**b**), m = 2 (**c**), and m = 3 (**d**) in haze environments containing varying components: meteoric, dust-type, soot, and sulfate particles.

Higher OAM modes, characterized by a broader spatial energy distribution, result in lower local intensity at particle locations. This localized reduction in intensity weakens the interaction between the beam and individual particles, effectively decreasing the probability of scattering events. However, it is important to emphasize that while the local interaction strength varies, the overall attenuation process remains consistent with the single scattering approximation. Conversely, lower OAM modes concentrate energy within smaller regions, increasing the local intensity and thereby enhancing the likelihood of scattering and attenuation.

For the s = 0 (non-vortex) beam, soot particles have a significant impact on transmittance due to their high absorption coefficient, which stems from their larger imaginary component of the refractive index compared to other particle types. This results in pronounced transmission loss. In contrast, dust-like and meteoric particles exhibit lower absorption, leading to a more moderate reduction in transmittance. Sulfate particles, being weakly absorptive, cause minimal radiation attenuation, particularly at higher OAM modes where the energy is more spatially dispersed.

Crucially, within the framework of the single scattering approximation, radiation attenuation adheres to the Beer–Lambert law, meaning that transmittance follows an exponential decay as a function of propagation distance L. While the spatial intensity distribution of the beam affects the effective scattering coefficient—which governs the rate of attenuation—this influence does not contradict the exponential decay prescribed by the Beer–Lambert law. Instead, it modifies the attenuation rate by altering the local interaction strength between the beam and the medium, without deviating from the fundamental exponential dependence of transmittance on path length.

4. Conclusions

This study investigates the single scattering behavior of vector BG beams in winter haze environments, with a focus on the effects of ice-coated particles. Using the Generalized Lorenz–Mie Theory, we explore how the transition from water to ice coatings on haze particles alters their optical scattering properties. Our findings reveal that ice-coated particles notably modify both the scattering and extinction efficiencies when compared to their water-coated counterparts, highlighting the critical influence of surface morphology and variations in the refractive index on light-particle interactions.

We further quantify the attenuation of BG beams in hazy atmospheres, demonstrating that higher particle concentrations significantly enhance scattering, which leads to pronounced reductions in transmittance, particularly at shorter wavelengths. Additionally, this study investigates the interaction of BG beams with varying OAM modes across diverse particle types, including meteoric, dust-type, soot, and sulfate-type particles. Notably, an increase in the OAM value correlates with a reduction in the extinction efficiency factor. This phenomenon is attributed to the broader spatial energy distribution inherent in higher OAM modes, which spread the energy over a larger area. As a result, the local intensity at the particle location diminishes, weakening the interactions between the beam and individual particles. Importantly, while these localized intensity effects influence the interaction dynamics, the overall scattering behavior remains consistent with the single scattering approximation. The attenuation process continues to adhere to the Beer–Lambert law, with the extinction coefficient being governed by the spatial energy distribution of the beam, rather than any fundamental deviation from the exponential decay model.

These findings underscore the intricate interplay between particle morphology, composition, and beam characteristics in shaping scattering and transmittance phenomena. By providing critical insights into how particle types, OAM modes, and atmospheric conditions impact light propagation, this study contributes valuable guidance for designing optical communication and sensing systems in particulate-laden environments.

Author Contributions: These authors contributed equally to this work, Y.Y. and Y.C.; investigation, Y.Y. and Y.C.; writing—original draft preparation, Y.Y.; methodology, Y.C. and M.C.; software, W.J.; supervision, L.G. All authors have read and agreed to the published version of the manuscript.

Funding: This research was funded by the National Natural Science Foundation of China, grant number U20B2059, 62231021, 61621005, 62201613, and the Shanghai Aerospace Science and Technology Innovation Foundation, grant number SAST-2022-069.

Institutional Review Board Statement: Not applicable.

Informed Consent Statement: Not applicable.

Data Availability Statement: Data are contained within the article.

Acknowledgments: The authors would like to thank the editor and anonymous reviewers who handled our paper.

Conflicts of Interest: The authors declare no conflicts of interest.

References

1. Bennett, C.A. *Principles of Physical Optics*; John Wiley & Sons: Hoboken, NJ, USA, 2022.
2. Bohren, C.F.; Huffman, D.R. *Absorption and Scattering of Light by Small Particles*; John Wiley & Sons: Hoboken, NJ, USA, 2008.
3. Kokhanovsky, A. Optical Properties of Terrestrial Clouds. *Earth-Sci. Rev.* **2004**, *64*, 189–241. [CrossRef]
4. Grabner, M.; Kvicera, V. Multiple Scattering in Rain and Fog on Free-Space Optical Links. *J. Light. Technol.* **2014**, *32*, 513–520. [CrossRef]
5. Van de Hulst, H.C. *Light Scattering by Small Particles*; Courier Corporation: North Chelmsford, MA, USA, 1981.
6. Lorenz, L. Upon the Light Reflected and Refracted by a Transparent Sphere. *Vidensk. Selsk. Shrifter* **1890**, *6*, 61–62.

7. Mie, G. Articles on the Optical Characteristics of Turbid Tubes, Especially Colloidal Metal Solutions. *Ann. Phys.-Berl.* **1908**, *330*, 377–445. [CrossRef]
8. Gouesbet, G.; Maheu, B.; Gréhan, G. Light Scattering from a Sphere Arbitrarily Located in a Gaussian Beam, Using a Bromwich Formulation. *J. Opt. Soc. Am. A* **1988**, *5*, 1427–1443. [CrossRef]
9. Hess, M.; Koepke, P.; Schult, I. Optical Properties of Aerosols and Clouds: The Software Package OPAC. *Bull. Amer. Meteorol. Soc.* **1998**, *79*, 831–844. [CrossRef]
10. Han, Q.; Rossow, W.B.; Lacis, A.A. Near-Global Survey of Effective Droplet Radii in Liquid Water Clouds Using ISCCP Data. *J. Clim.* **1994**, *7*, 465–497. [CrossRef]
11. Shi, C.; Guo, L.; Cheng, M. Aerosol Scattering of Vortex Beams Transmission in Hazy Atmosphere. *Opt. Express* **2020**, *28*, 28072–28084. [CrossRef] [PubMed]
12. Chervet, P.; Lavigne, C.; Roblin, A.; Bruscaglioni, P. Effects of Aerosol Scattering Phase Function Formulation on Point-Spread-Function Calculations. *Appl. Opt.* **2002**, *41*, 6489–6498. [CrossRef]
13. Sloane, C.S. Optical Properties of Aerosols of Mixed Composition. *Atmos. Environ.* **1984**, *18*, 871–878. [CrossRef]
14. He, J.; Gong, S.; Zhou, C.; Lu, S.; Wu, L.; Chen, Y.; Yu, Y.; Zhao, S.; Yu, L.; Yin, C. Analyses of Winter Circulation Types and Their Impacts on Haze Pollution in Beijing. *Atmos. Environ.* **2018**, *192*, 94–103. [CrossRef]
15. Porfirev, A.P.; Kirilenko, M.S.; Khonina, S.N.; Skidanov, R.V.; Soifer, V.A. Study of Propagation of Vortex Beams in Aerosol Optical Medium. *Appl. Opt.* **2017**, *56*, E8–E15. [CrossRef]
16. Zhang, Y.; Belić, M.; Wu, Z.; Zheng, H.; Lu, K.; Li, Y.; Zhang, Y. Soliton pair generation in the interactions of Airy and nonlinear accelerating beams. *Opt. Lett.* **2013**, *38*, 4585–4588. [CrossRef] [PubMed]
17. Zhang, D.; Liu, X.; Yang, L.; Li, X.; Zhang, Z.; Zhang, Y. Modulated vortex six-wave mixing. *Opt. Lett.* **2017**, *42*, 3097–3100. [CrossRef] [PubMed]
18. Yuan, X.; Xu, Q.; Lang, Y.; Jiang, X.; Xu, Y.; Chen, X.; Han, J.; Zhang, X.; Han, J.; Zhang, W. Tailoring spatiotemporal dynamics of plasmonic vortices. *Opto-Electron. Adv.* **2023**, *6*, 220133-1. [CrossRef]
19. Zhang, Z.; Li, G.; Liu, Y.; Wang, H.; Hoenders, B.J.; Liang, C.; Cai, Y.; Zeng, J. Robust measurement of orbital angular momentum of a partially coherent vortex beam under amplitude and phase perturbations. *Opto-Electron. Sci.* **2024**, *3*, 240001-1. [CrossRef]
20. Zhou, Y.; Liu, T.; Dai, C.; Wang, D.; Zhou, L. Functionality multiplexing in high-efficiency metasurfaces based on coherent wave interferences. *Opto-Electron. Adv.* **2024**, *7*, 240086-1. [CrossRef]
21. Zhao, S.; Zhang, W.; Wang, L.; Li, W.; Gong, L.; Cheng, W.; Chen, H.; Gruska, J. Propagation and Self-Healing Properties of Bessel-Gaussian Beam Carrying Orbital Angular Momentum in an Underwater Environment. *Sci. Rep.* **2019**, *9*, 2025. [CrossRef] [PubMed]
22. Cheng, M.; Guo, L.; Li, J.; Zhang, Y. Channel Capacity of the OAM-Based Free-Space Optical Communication Links with Bessel-Gauss Beams in Turbulent Ocean. *IEEE Photonics J.* **2016**, *8*, 7901411. [CrossRef]
23. Ji, J.; Zheng, Z.; Zhu, J.; Wang, L.; Wang, X.; Zhao, S. Bessel-Gaussian Beam-Based Orbital Angular Momentum Holography. *Chin. Phys. B* **2024**, *33*, 014204. [CrossRef]
24. Fu, S.; Wang, T.; Zhang, Z.; Zhai, Y.; Gao, C. Non-Diffractive Bessel-Gauss Beams for the Detection of Rotating Object Free of Obstructions. *Opt. Express* **2017**, *25*, 20098–20108. [CrossRef] [PubMed]
25. Huang, K.; Shi, P.; Cao, G.W.; Li, K.; Zhang, X.B.; Li, Y.P. Vector-Vortex Bessel-Gauss Beams and Their Tightly Focusing Properties. *Opt. Lett.* **2011**, *36*, 888–890. [CrossRef]
26. Vaity, P.; Rusch, L. Perfect Vortex Beam: Fourier Transformation of a Bessel Beam. *Opt. Lett.* **2015**, *40*, 597–600. [CrossRef]
27. Mphuthi, N.; Botha, R.; Forbes, A. Are Bessel beams resilient to aberrations and turbulence? *JOSA A* **2018**, *35*, 1021–1027. [CrossRef]
28. Cheng, M.; Guo, L.; Li, J.; Huang, Q. Propagation Properties of an Optical Vortex Carried by a Bessel-Gaussian Beam in Anisotropic Turbulence. *J. Opt. Soc. Am. A* **2016**, *33*, 1442–1450. [CrossRef]
29. Shi, C.; Guo, L.; Cheng, M.; Li, R. Scattering of a High-Order Vector Bessel-Gaussian Beam by a Spherical Marine Aerosol. *J. Quant. Spectrosc. Radiat. Transf.* **2021**, *265*, 107552. [CrossRef]
30. Shi, C.; Cheng, M.; Guo, L. Attenuation Characteristics of Bessel-Gaussian Vortex Beam by a Wet Dust Particle. *Opt. Commun.* **2022**, *514*, 128138. [CrossRef]
31. Dong, K.; Jiang, W.; Cheng, M.; Shi, C.; Cao, Y.; Guo, L. Attenuation of Bessel Vortex Beam Transmission in the Rain Environment. *J. Quant. Spectrosc. Radiat. Transfer* **2023**, 108620. [CrossRef]
32. Valdivia, N.L.; Votto, L.F.; Gouesbet, G.; Wang, J.; Ambrosio, L.A. Bessel-Gauss Beams in the Generalized Lorenz-Mie Theory Using Three Remodeling Techniques. *J. Quant. Spectrosc. Radiat. Transf.* **2020**, *256*, 107292. [CrossRef]
33. Cheng, M.J.; Cao, Y.C.; Ren, K.F.; Zhang, H.; Guo, L.X. Generalized Lorenz-Mie Theory and Simulation Software for Structured Light Scattering by Particles. *Front. Phys.* **2024**, *12*, 1354223. [CrossRef]
34. Kerker, M. *The Scattering of Light and Other Electromagnetic Radiation*; Harcourt Brace Jovanovich: New York, NY, USA, 1969.

35. Brewster, M.Q.; Tien, C.L. Radiative transfer in packed fluidized beds: Dependent versus independent scattering. *J. Heat Transf.* **1982**, *104*, 573–579. [CrossRef]
36. Deirmendjian, D. ; *Electromagnetic Scattering on Spherical Polydispersions*; American Elsevier Publishing Company: New York, NY, USA, 1969.

Disclaimer/Publisher's Note: The statements, opinions and data contained in all publications are solely those of the individual author(s) and contributor(s) and not of MDPI and/or the editor(s). MDPI and/or the editor(s) disclaim responsibility for any injury to people or property resulting from any ideas, methods, instructions or products referred to in the content.